Optics Communications 366 (2016) 354–361

Contents lists available at ScienceDirect

Optics Communications

journal homepage: www.elsevier.com/locate/optcom

Invited Paper

Quadrature amplitude modulation (QAM) using binary-driven coupling-modulated rings

Samira Karimelahi *, Ali Sheikholeslami

Department of Electrical and Computer Engineering, University of Toronto, Ontario, Canada M5S 3G4

ARTICLE INFO

Article history:
Received 21 September 2015
Received in revised form
1 January 2016
Accepted 4 January 2016
Available online 8 January 2016

Keywords:
Silicon photonics
Waveguide modulators
Optical communications
QAM modulator
Ring resonator
Opto-electronics

ABSTRACT

We propose and fully analyze a compact structure for DAC-free pure optical QAM modulation. The proposed structure is the first ring resonator-based DAC-free QAM modulator reported in the literature, to the best of our knowledge. The device consists of two segmented add-drop Mach Zehnder interferometer-assisted ring modulators (MZIARM) in an IQ configuration. The proposed architecture is investigated based on the parameters from SOI technology where various key design considerations are discussed. We have included the loss in the MZI arms in our analysis of phase and amplitude modulation using MZIARM for the first time and show that the imbalanced loss results in a phase error. The output level linearity is also studied for both QAM-16 and QAM-64 not only based on optimizing RF segment lengths but also by optimizing the number of segments. In QAM-16, linearity among levels is achievable with two segments while in QAM-64 an additional segment may be required.

1. Introduction

Advanced optical modulation formats have received more attention recently due to the rising need for higher bandwidth and advances in coherent detection [1]. The higher spectral efficiency of modulation formats such as pulse amplitude modulation (PAM) and quadrature amplitude modulation (QAM), compared to on-off keying (OOK), makes them more suitable for translating electrical data to optical output in a transmitter. In particular, QAM combines multi-amplitude and multi-phase modulation, and has been widely used for high-speed communication.

There are several possible configurations for QAM modulator. These can be divided into two main categories: (1) modulators requiring multi-level electrical signal and (2) modulators requiring binary electrical signal. One of the widely used architectures that fits into the first category is an IQ optical modulator where each of the I- and Q-arm of a Mach–Zehnder interferometer (MZI) consists of a MZI modulator driven by multi-level electrical signals [2,3]. Another example that also needs multi-level driver signal is cascading an MZI modulator with a phase modulator (PM) [3,4]. However, due to the complexity of generating linear and high-speed multi-level electrical signals, it is more desirable to generate multi-level amplitude and phase, both in the optical domain.

There have been several proposed architectures for binary-driven QAM-16 such as quad parallel MZI modulator [5] and two cascaded IQ optical modulators [6], but both schemes require four (instead of two) modulators that add to the cost and complexity. Another binary-driven architecture uses an IQ modulator with imbalanced power-splitting ratio couplers in the input of both nested MZIs [7]. This requires two tunable MZIs instead of Y junctions and increases the device size further. A more promising QAM configuration was demonstrated using segmented MZIs in the silicon-insulator-silicon capacitor (SISCAP) [8]. Substituting an MZI by an MZI-assisted ring modulator (MZIARM) leads to a much shorter RF length and lower required driving voltage [9]. We recently proposed PAM signaling based on all-pass segmented MZIARM [10]. Also, MZIARM in add-drop configuration was demonstrated recently to work as a low-chirp binary phase-shift keying (BPSK) modulator [11]. In [11], π phase shift at the output of the drop port was achieved by flipping sign of cross coupling coefficient at the drop port.

In this paper, we propose M-ary QAM modulator that consists of two add-drop MZIARMs with multi-segment RF region at the drop port in IQ configuration. We show that using add-drop MZIARM with multi-segment active region in the drop port not only will induce the π phase shift but also will generate the multi-level modulation pure optically and eliminates the requirement for DAC in the electrical driver. The device is also fully analyzed in SOI process [12]. The MZI in the MZIARM is considered to be lossy and phase and amplitude modulation are analyzed accordingly. The impact of the imbalanced loss of MZI arms in MZIARM on the phase modulation is taken into account for the first time to the best of our knowledge. The proposed device operation is also

* Corresponding author.
E-mail address: samira@ece.utoronto.ca (S. Karimelahi).

http://dx.doi.org/10.1016/j.optcom.2016.01.006
0030-4018/

validated by assessing transient response in the non-quasi-static mode of operation. Also, the on resonance optical transmission at the drop port is considered and assessed for optimizing level linearity. Hence, the principle of operation of a multi-segment add-drop MZIARM is provided together with the simulation results of QAM-16 and QAM-64 constellations where in each case, the output level linearity is studied. In addition, the number of segments in add-drop MZIARM is also optimized.

2. Device proposal and theoretical background

The proposed QAM-16 modulator schematic is shown in Fig. 1 in a push–pull driven scheme. The modulator consists of an add-drop MZIARM in I-arm and another add-drop MZIARM cascaded with a thermal tuner phase shifter targeted for $\pi/2$ phase shift, in the Q-arm of the MZI. Each of the add-drop MZIARM consists of the 2-segment RF phase shifters for active phase modulation and a thermal tuner to bias the device in the desired DC operating point and maintain the resonance wavelength of the ring resonator. Although in add-drop MZIARM, the coupling coefficient modulation at either the through or drop ports can be used for phase modulation, the drop port is selected here as it leads to a more efficient modulation [11]. Also, in the through port of each of these add-drop MZIARMs, there are small thermally tunable MZIs that work as couplers. However, these two MZIs could be replaced with simple directional couplers if the design and fabricated coupling coefficient match. This configuration is easily extendible to QAM-2^{2N}, $N \geq 2$, by using minimum N active segments in each arm, where more than N segments may be required for linearity, as will be discussed in Section 5.

Although the proposed device can be implemented by any free-carrier dispersion-based configurations, e.g. pn/pin diode or SIS-CAP [8], here, for the proof of concept, simulations are based on the parameters provided by Institute of Microelectronics (IME) /A*STAR [13] for an SOI process [12].

To provide insight into the device operation, we first briefly describe the operation principle of a single segment add-drop MZIARM. Assuming quasi-static mode of operation, the device can be analyzed using the steady state model [14]. The non-quasi-static mode of operation will be investigated later in Section 4. The electric field transmissions at the through and the drop ports of an add-drop ring resonator in the steady state are given by [11,15]:

$$T_{dr} = \kappa_1^* \kappa_2^* \frac{\sqrt{a_{ring}}\,\exp(-i\theta/2)}{1 - a_{ring} t_1^* t_2 \exp(-i\theta)},$$
$$T_{th} = \frac{t_1 - t_2 a_{ring}\exp(-i\theta)}{1 - a_{ring} t_1^* t_2 \exp(-i\theta)}. \quad (1)$$

where θ is the round-trip phase shift including the phase shift through the coupler, a_{ring} is the ring transmissivity, and $t_1(\kappa_1)$ and $t_2(\kappa_2)$ are the through (cross) coupling coefficients in the through and the drop ports, respectively. By employing an MZI as a tunable coupler in the drop port, as shown in Fig. 1, t_2 and κ_2 can be calculated from $\mathbf{C}\times\mathbf{P}\times\mathbf{C}$, where $\mathbf{C} = \begin{bmatrix} 1/\sqrt{(2)} & j/\sqrt{(2)} \\ j/\sqrt{(2)} & 1/\sqrt{(2)} \end{bmatrix}$ is a transfer matrix for a 50–50 directional coupler and $\mathbf{P} = \begin{bmatrix} a_{MZI}e^{-j\phi_1} & 0 \\ 0 & a_{MZI}e^{-j\phi_2} \end{bmatrix}$ is the propagation matrix of the phase shifters in MZI arms, assuming equal loss of a_{MZI}. Here, ϕ_1 and ϕ_2 are the phase accumulation in the top and the bottom arms. Based on this transfer matrix formulation, we have the following equations:

$$t_2 = -ia_{MZI}\sin\left(\frac{\Delta\phi}{2}\right),$$
$$\kappa_2 = ia_{MZI}\cos\left(\frac{\Delta\phi}{2}\right). \quad (2)$$

Here, $\Delta\phi = \phi_1 - \phi_2 = \phi_0 + \Delta\phi'$ is the phase difference between MZI arms, ϕ_0 is the DC bias phase, and $\Delta\phi'$ is the phase accumulation differences through the active region.

The static power transmissions of a silicon-based add-drop MZIARM at the drop and through ports on resonance, $\theta = 2m\pi$, m an integer, are shown in Fig. 2. In this example, the modulator is considered to have a round-trip length of 220 μm and propagation loss of 2 dB/cm corresponding to $a_{ring} = 0.995$, with $|t_1|$ taken to be 0.95 and assuming $a_{MZI} = 0.985$ and $n_{eff} = 2.44$. Note that these parameters are merely to show device operation principles and are not representative of a real device (foundry-based examples will be presented in the next sections). Considering that the device operates at T_{dr} null point ($\phi_0 = \pi$), a phase flip of π at the output occurs when crossing the transmission minimum. This is due to the fact that κ_2 switches sign as soon as the null point is crossed [11]. As shown in Fig. 2, modulator operation between the two peaks of T_{dr} corresponds to phase change of $2\Delta\phi'_{peak}$ where $|\Delta\phi'_{peak}|$ is the phase accumulation in the active region at T_{dr} peaks. This phase shift is much smaller than that required in the MZI modulator (dotted line in Fig. 2) for BPSK for the same distance between the constellation points. However, the maximum achievable transmission is higher for the MZI modulator than the one in MZIARM at drop port.

The locations of $|T_{dr}|$ peaks can be calculated by solving $\partial|T_{dr}|/\partial t_2 = 0$ which results in $|t_2| = a_{MZI}^2 a_{ring}|t_1|$ and equivalently, $\kappa_2 = \pm ia_{MZI}\sqrt{1 - a_{MZI}^2 a_{ring}^2|t_1|^2}$. From Eq. (2), $\Delta\phi'_{peak}$ is found to be $|\pi - 2\sin^{-1}(a_{MZI}a_{ring}|t_1|)|$ which shows that the closer $a_{MZI}a_{ring}|t_1|$ is to 1, the closer the two peak locations will be and consequently, the less required phase modulation is. According to Eq. (1), transmission at the through port becomes zero at the critical coupling condition which occurs when $|t_2| = |t_1|/a_{ring}$ corresponding

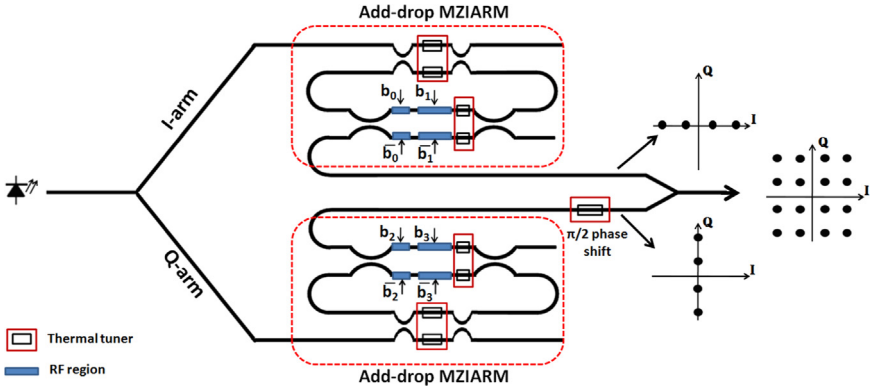

Fig. 1. Schematic of the proposed QAM-16 modulator using two segmented add-drop MZIARMs in IQ configuration.

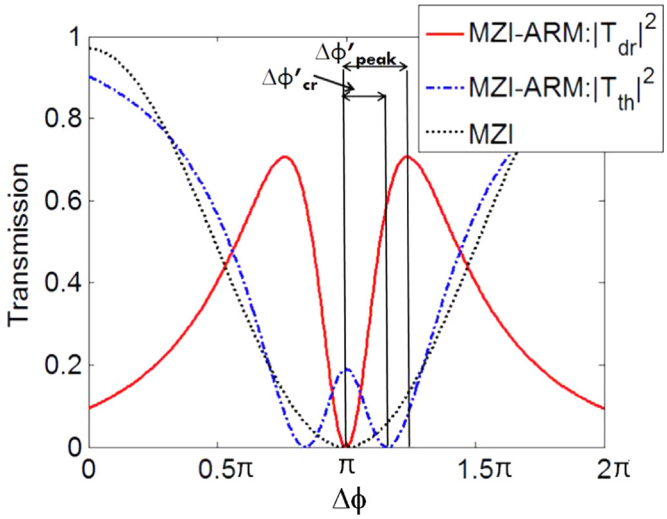

Fig. 2. On-resonance power transmission versus $\Delta\phi$ of an MZI, and of an add-drop MZIARM at the through and the drop ports.

to the active region phase accumulation of $\Delta\phi'_{cr}$, which is equal to $|\pi - 2\sin^{-1}(|t_1|/(a_{MZI}a_{ring}))|$. Only for $a_{MZI}a_{ring} = 1$, $\Delta\phi'_{cr}$ is equal to $\Delta\phi'_{peak}$ (Fig. 2). Here, the obtained equations for the single segment add-drop MZIARM represent a more complete version of the formulae presented in [11]. In the current model, we have taken the effect of MZI arm loss into account. The derived formulation shows that this loss term leads to different effects compared to the ring resonator round-trip loss.

3. Active region segmentation in add-drop MZIARM

By segmenting the MZIARM active region into L_1 and L_2 corresponding to the least significant bit (b_0) and the most significant bit (b_1), respectively, $\Delta\phi'$ in Eq. (2) can take four possible values depending on the input bit sequence of b_1b_0 similar to PAM-4 [10]. However, here, due to the symmetry around π, two out of four cases have the same absolute values but opposite signs. The values of $\Delta\phi'$ can be calculated from

$$\begin{bmatrix}\Delta\phi'_3\\ \Delta\phi'_2\\ \Delta\phi'_1\\ \Delta\phi'_0\end{bmatrix} = \begin{bmatrix}\Delta\phi'_3\\ \Delta\phi'_2\\ -\Delta\phi'_2\\ -\Delta\phi'_3\end{bmatrix} = \begin{bmatrix}r+1\\ r-1\\ -r+1\\ -r-1\end{bmatrix} \times M \times L_1. \tag{3}$$

Here, $r = L_2/L_1$ and $M = 2\pi/\lambda_{res} \times \Delta n_{eff}(V)$, where λ_{res} is the resonance wavelength and $\Delta n_{eff}(V)$ is the refractive index change as a function of driving voltage (V).

Based on this, a 2-segment add-drop MZIARM is simulated electro-optically to study the device performance. Loss and effective refractive index of the active regions as a function of voltage are calculated using a commercial device and optical simulator [16] and passive waveguide loss is considered to be 2 dB/cm. Fig. 3a and b shows the simulated change in effective index and pn junction loss versus reverse bias voltage that are used here. Total loss at 0 V is 7 dB/cm. The 2-segment add drop MZIARM is simulated using the transfer matrix formalism of the MZI together with the ring round-trip equation. Breaking the assumption of having equal losses in the MZI arms, the propagation matrix of MZI should be considered as $\mathbf{P} = \begin{bmatrix} a_1 e^{-j\phi_1} & 0 \\ 0 & a_2 e^{-j\phi_2}\end{bmatrix}$, where a_1 and a_2 are the losses in the top and the bottom arms of the MZI, respectively. Due to the loss modulation accompanying the refractive index modulation in the plasma dispersion effect, similar to four possible values of $\Delta\phi'$ in Eq. (3), there will be four slightly different propagation losses at each arm of the MZI depending on the input bit sequence (b1b0). In this case, $a_1 = [a_{11}\ a_{12}\ a_{13}\ a_{14}]$ and a_2 is a_1 with the reverse order due to the push–pull driven configuration. Fabrication imperfection will also add to this loss inequality in MZI arms, however, due to the small size of the device it will be less probable. As a result of the loss imbalance in the MZI arms, the through and cross coupling coefficient formalization and therefore T_{dr} and T_{th} equations will be slightly different from what were presented in Eqs. (2) and (1). The effect of this non-equal loss will be explained later in the paper.

As shown in Eq. (3), $\Delta\phi'_3$ is determined for a selected total segment length (L_t) and applied voltage. Larger $\Delta\phi'_3$ leads to a higher maximum value of T_{dr}. One way of increasing $\Delta\phi'_3$ is to increase L_t at the constant applied voltage. Fig. 4a shows maximum $|T_{dr}|$ as a function of L_t for the applied voltage of 4.4 V_{pp} considering reverse-biased pn junction. For each value of L_t, t_1 is optimized to give the maximum $|T_{dr}|$. As shown in Fig. 4a, T_{dr} increases more sharply at the smaller L_t while it nearly saturates at the larger L_t. This saturation is a consequence of a loss increase as a

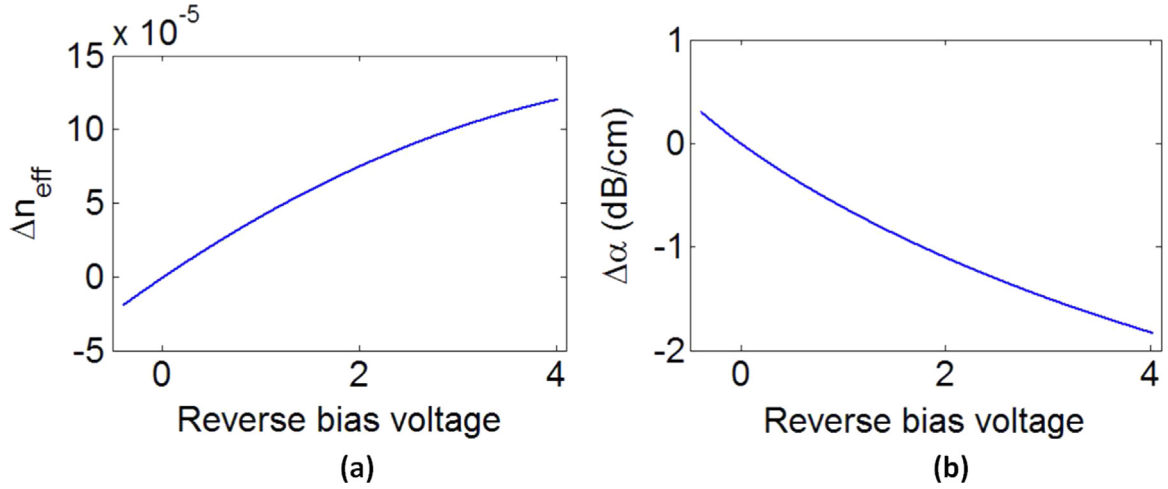

Fig. 3. Change in (a) effective index (b) pn junction loss versus reverse bias voltage.

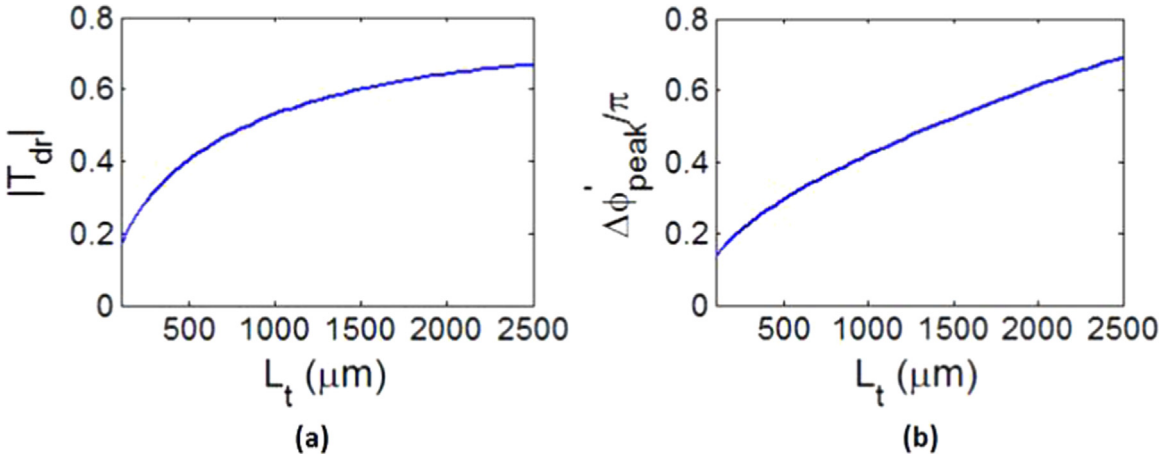

Fig. 4. (a) Amplitude of the field transmission at the output of the drop port. (b) Peak locations of $|T_{dr}|$ ($\Delta\phi'_{peak}$) versus L_t.

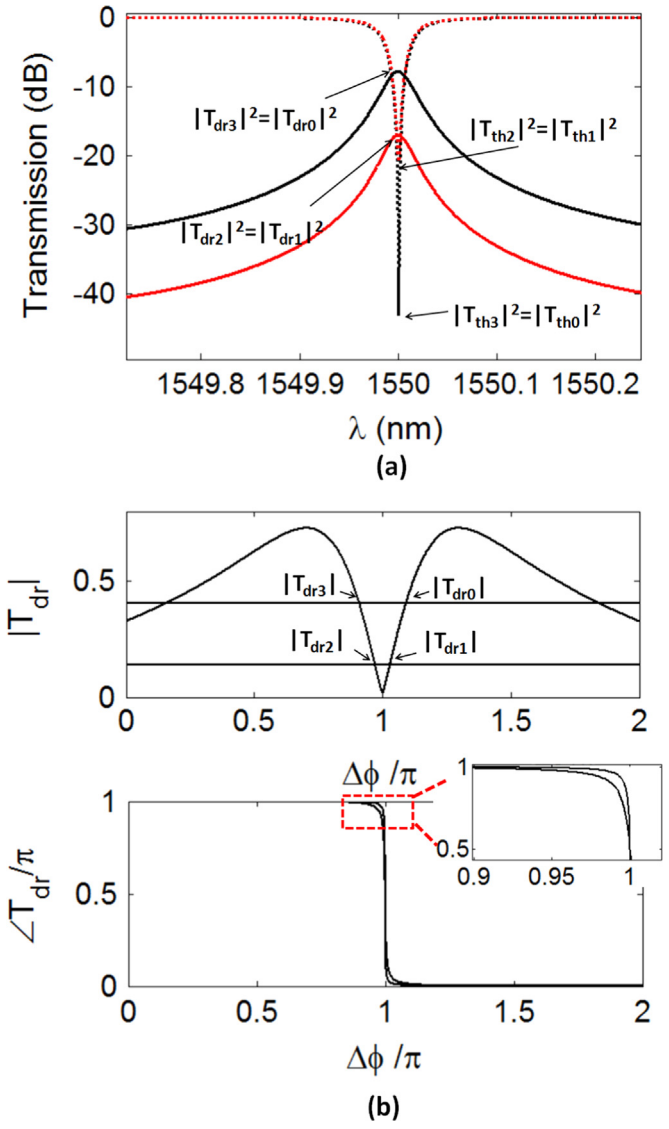

Fig. 5. A 2-segment MZIARM (a) optical power transmission spectra for the drop and through ports and (b) amplitude and phase of the field transmission at the output of the drop port versus normalized $\Delta\phi$.

function of length. Moreover, as shown in Fig. 4b, larger L_t leads to $\Delta\phi'_{peak}$ further away from π, resulting in a less steep transfer function which lowers modulation efficiency. As such, choice of L_t is a trade off between the maximum T_{dr} and the efficiency. Here, we have selected $L_t = 500\,\mu m$ for all the simulations of the reverse-biased device.

Fig. 5a shows the power transmission spectra of the drop and through ports of the 2-segment add-drop MZIARM assuming reverse biased-pn junction with $r=2$, $t_1 = 0.94$ and $V_{pp} = 4.4$ V. These values result in modulation of $|\kappa_2|$ between 0.046 and 0.14. An ER of about 9 dB is observed between the maximum and minimum on-resonance transmission at the drop port. Fig. 5b shows the amplitude and phase of the on-resonance field transmission at the drop port versus normalized $\Delta\phi$. The on-resonance field transmission amplitudes are indicated as $|T_{dr0}|$, $|T_{dr1}|$, $|T_{dr2}|$, and $|T_{dr3}|$. According to Fig. 5b, the effect of the difference in loss of the MZI two arms has negligible effect on $|T_{dr}|$. However, the imbalanced loss impact on the phase of the field transmission at the drop port is more significant. Also, $\angle T_{dr}$ deviates from 0 and π in vicinity of $\Delta\phi/\pi = 1$. In the case of non-equal loss in two MZI arms, t_2 and κ_2^* in Eq. (1) should be respectively replaced by

$$t_2 \rightarrow \frac{1}{2}(a_1+a_2)\left[\frac{(a_2-a_1)}{(a_2+a_1)}\cos\left(\frac{\Delta\phi}{2}\right) - i\sin\left(\frac{\Delta\phi}{2}\right)\right], \tag{4a}$$

$$\kappa_2^* \rightarrow -\frac{i}{2}(a_1+a_2)\left[\cos\left(\frac{\Delta\phi}{2}\right) + i\frac{(a_2-a_1)}{(a_2+a_1)}\sin\left(\frac{\Delta\phi}{2}\right)\right] \tag{4b}$$

where $|(a_2-a_1)/(a_2+a_1)| \ll 1$. If $a_1 = a_2 = a$, then Eq. (4a) and (4b) becomes the same as the t_2 and κ_2^* in Eq. (1). Close to $\Delta\phi/\pi = 1$, where the modulator is operating, Eq. (4a) can be approximated by $-ia\sin(\Delta\phi/2)$. However, in this region, the term $i(a_2-a_1)/(a_2+a_1)\sin(\Delta\phi/2)$ in Eq. (4b) will be comparable with $\cos(\Delta\phi/2)$ and therefore κ_2^* becomes a complex number rather than the pure imaginary value in Eq. (2). Consequently, modulation of $\Delta\phi$ will not result in the complete sign flip in T_{dr} and this will result in a phase error. As a_1 and a_2 have four different values based on b_1b_0, there are four phase curves where two of them are clearly observable (dotted box in Fig. 5b). In the current example, the maximum phase error is about 0.02π, but could be larger depending on the active region length and loss-voltage dependency. The phase error will affect the QAM constellation as will be discussed in the next section.

4. Non-quasi-static analysis

So far, we focused on the quasi-static mode of operation where closed-form forumlae can describe the operation of the proposed

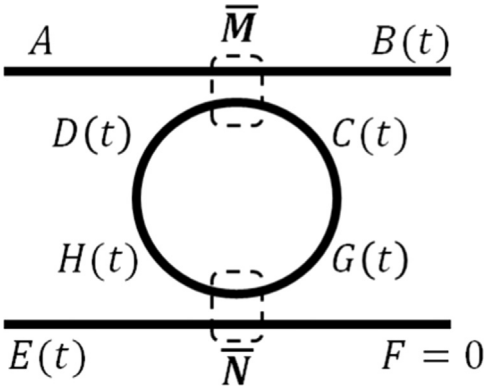

Fig. 6. Schematic of an add-drop coupling-modulated ring resonator.

QAM modulator. In order to show that the proposed device operates in the non-quasi-static mode as well, we carried out a time domain simulation. For simplicity, ring modulator self-heating effect due to the free-carrier absorption [17] is not considered. Here, we consider QAM-16 which includes two 2-segment add-drop MZIARMs. Fig. 6 shows a simplified schematic of one of the MZIARMs where A is the amplitude of a continues-wave input and B, C, D, G, H, and E are the time-dependent slowly-varying envelopes of the electric field at the locations shown. The input at the add port, F, is zero. Also shown are the coupling matrices at the through and drop port indicated as $\bar{\mathbf{M}}$ and $\bar{\mathbf{N}}$, respectively. Similar to previous sections, the MZI modulator is consider to be at the drop port. All the parameters taken for this simulation are similar to those used in Section 3. The device is driven by a 4.4 V_{pp} pseudo-random input bit stream at 30 Gb/s where the modulation frequency is about 10 × higher than the cavity linewidth. At this rate, the quasi-static assumption is not valid, which necessitates the current time domain simulation. The input bit stream is first filtered by a 54 GHz low-pass RC filter based on the junction capacitance and series resistance in the selected technology. Then, based on the voltage-dependent refractive index and loss shown in Fig. 3, the time-dependent propagation matrix, $\bar{\mathbf{P}}$, is found. From this, $\bar{\mathbf{M}} = \mathbf{C} \times \mathbf{P} \times \mathbf{C}$ is calculated. At the thought port, the time-independent coupling matrix $\bar{\mathbf{N}}$ is $\begin{bmatrix} t_1 & \kappa_1 \\ -\kappa_1^* & t_1^* \end{bmatrix}$. Based on these coupling matrices, we have the following relations for the electric field envelops in Fig. 6:

$$\begin{bmatrix} B(t) \\ C(t) \end{bmatrix} = \bar{\mathbf{M}} \begin{bmatrix} A \\ D(t) \end{bmatrix}, \tag{5a}$$

$$\begin{bmatrix} H(t) \\ E(t) \end{bmatrix} = \bar{\mathbf{N}} \begin{bmatrix} G(t) \\ 0 \end{bmatrix}. \tag{5b}$$

Also, considering round-trip propagation time of τ, the following additional equations hold

$$G(t) = C(t - \tau/2)\sqrt{a_{ring}}e^{-j\frac{\theta}{2}}, \tag{6a}$$

$$D(t) = H(t - \tau/2)\sqrt{a_{ring}}e^{-j\frac{\theta}{2}}. \tag{6b}$$

Based on Eqs. (5a)–(6b), the electric field envelope at the drop port, $E(t)$, and T_{dr} can be calculated through an iterative method. Fig. 7 shows the calculated $\Delta\phi'$, κ_2 ($N(1, 2)$), and T_{dr} as a function of time. The device is modulated after being operated in the steady state for a few cycles. Four levels of $\Delta\phi'$ are illustrated in Fig. 7, as expected for 2-segment MZIARM. This results in four levels of

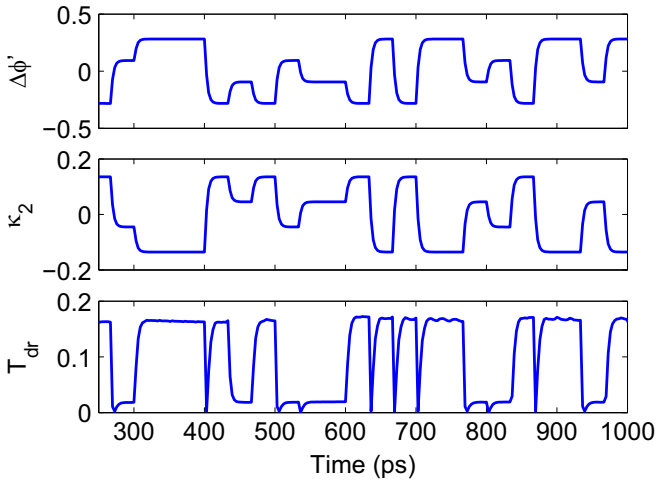

Fig. 7. Phase accumulation differences through the active regions, cross coupling coefficient at the drop port, and power transmission at the drop port versus time.

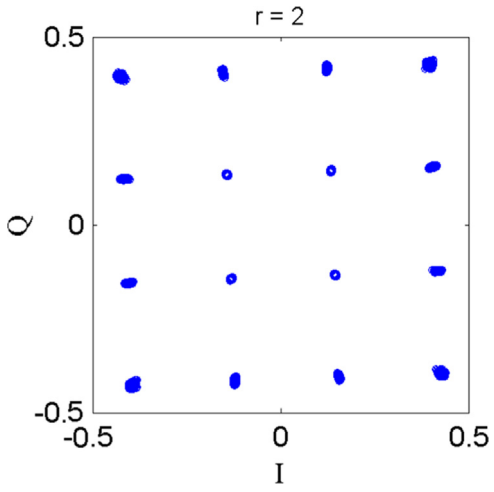

Fig. 8. Constellation diagram of QAM-16 for $L_t = 500\,\mu m$.

coupling coefficient at the drop port. As shown in Fig. 7, T_{dr} has two levels of amplitude as it is expected from Fig. 5 in quasi-static domain. In order to observe both phase and amplitude multi-leveling, constellation diagram is generated. Four independent bit streams of 4000 bits are applied to each active region in the QAM modulator shown in Fig. 1. Constellation diagram of QAM-16 for $r=2$ is generated and shown in Fig. 8. Deviation of the constellation points from vertical and horizontal line is due to the phase error as a result of loss imbalance between two arms of the MZI modulator as discussed in Section 3. Phase error also exists in the QAM modulator that is using MZI due to imbalanced arm losses and limited ER [18]. It will be shown in the next section that this deviation of constellation occurs in the quasi-static simulations as well.

5. Output level liniearity

Linearity of the QAM output levels can be studied through steady-state analysis. Even though the transient respond could potentially slightly change the levels, the methodology applied here is valid for exploring the effect of nonlinear curve of the add-drop MZIARM on the constellation of QAM-16. As can be seen from Eq. (3), $\Delta\phi'$ and the level distribution can be modified by adjusting

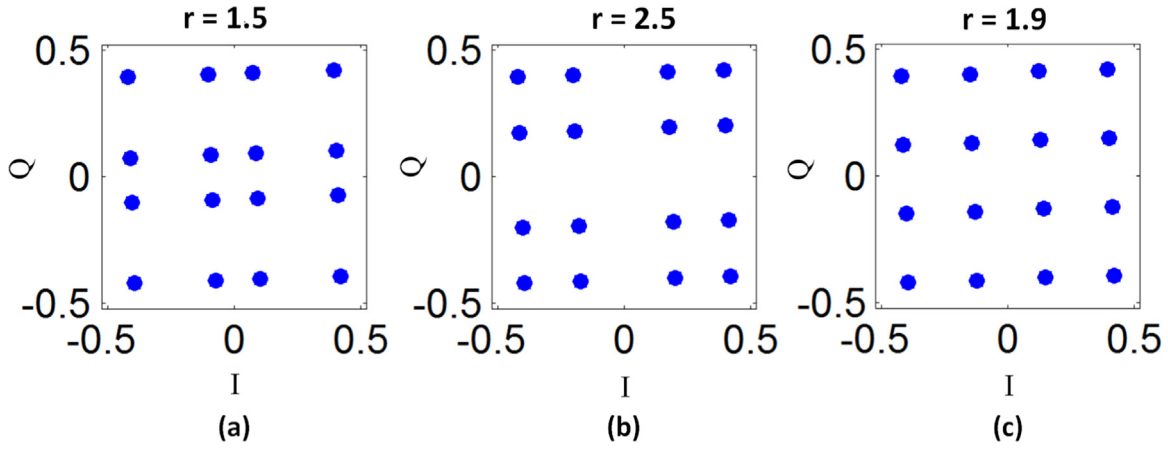

Fig. 9. QAM-16 constellation for $L_t = 500\ \mu m$ and for (a) $r=1.5$, (b) $r=2.5$, and (c) $r=1.9$.

the driving voltage and consequently Δn_{eff} and/or the segment length ratio. Here, we focus on optimizing the segment length ratio as adjusting the driving voltage for each segment may add to the driver circuit complexity and becomes less practical compared with adjusting the segment lengths. For a fixed L_t of 500 μm, the QAM-16 constellations are plotted for $r=1.5$ and 2.5 as shown in Fig. 9a and b. According to the figure, the constellation map significantly changes with variation of the segment ratio, r. Here, a certain r value can be found for an exact linear level distribution. Given $T_{dr3} = -T_{dr0}$ and $T_{dr1} = -T_{dr2}$ (Fig. 5b), for a fixed L_t, the only equation that should be satisfied to arrive at the linear levels is $T_{dr2} = T_{dr3}/3$. For the current example of $L_t = 500\ \mu m$, r is calculated to be around 1.9. This calculated value of 1.9 is close to binary-weighted ratio of 2, as the region of operation is almost in the linear part of $|T_{dr}|$–$\Delta\phi/\pi$ curve in Fig. 5b. The corresponding QAM-16 constellation is shown in Fig. 9c. The small tilt that exists in all constellations shown in Fig. 9 is due to the aforementioned phase error.

As shown here, linearly-spaced constellation can be achieved for QAM-16 using two RF segments in each arm of MZI in each MZIARM. However, for QAM-2^{2N}, $N \geq 3$, employing N segments does not lead to complete level linearity. As an example, in QAM-64, $\boldsymbol{\Delta\phi'}$ can be calculated from the following equation:

$$\boldsymbol{\Delta\phi'} = \begin{bmatrix} \Delta\phi_3' \\ \Delta\phi_2' \\ \Delta\phi_1' \\ \Delta\phi_0' \\ -\Delta\phi_0' \\ -\Delta\phi_1' \\ -\Delta\phi_2' \\ -\Delta\phi_3' \end{bmatrix} = \begin{bmatrix} r_3 + r_2 + 1 \\ r_3 + r_2 - 1 \\ r_3 - r_2 + 1 \\ r_3 - r_2 - 1 \\ -r_3 + r_2 + 1 \\ -r_3 + r_2 - 1 \\ -r_3 - r_2 + 1 \\ -r_3 - r_2 - 1 \end{bmatrix} \times M \times L_1 \tag{7}$$

where $r_2 = L_2/L_1$, $r_3 = L_3/L_1$. Now, consider $\boldsymbol{\Delta\phi'_{opt}}$ to be the column vector including 8 desired phase differences to get linear amplitude distribution in the I/Q-arm of the MZI. In order to achieve linearity, $\boldsymbol{\Delta\phi'}$ from Eq. (7) should approach $\boldsymbol{\Delta\phi'_{opt}}$, which results in 4 independent equations. However, embedding three RF segments in each arm of the MZI in the add-drop MZIARM leads to only three variables of L_t, r_2, and r_3. This is clearly not enough to get the exact linearly-distributed constellation. However, for a small dynamic range, where the operation region is in the linear part of the $|T_{dr}|$–$\Delta\phi/\pi$ curve, such as in the current example of reverse bias

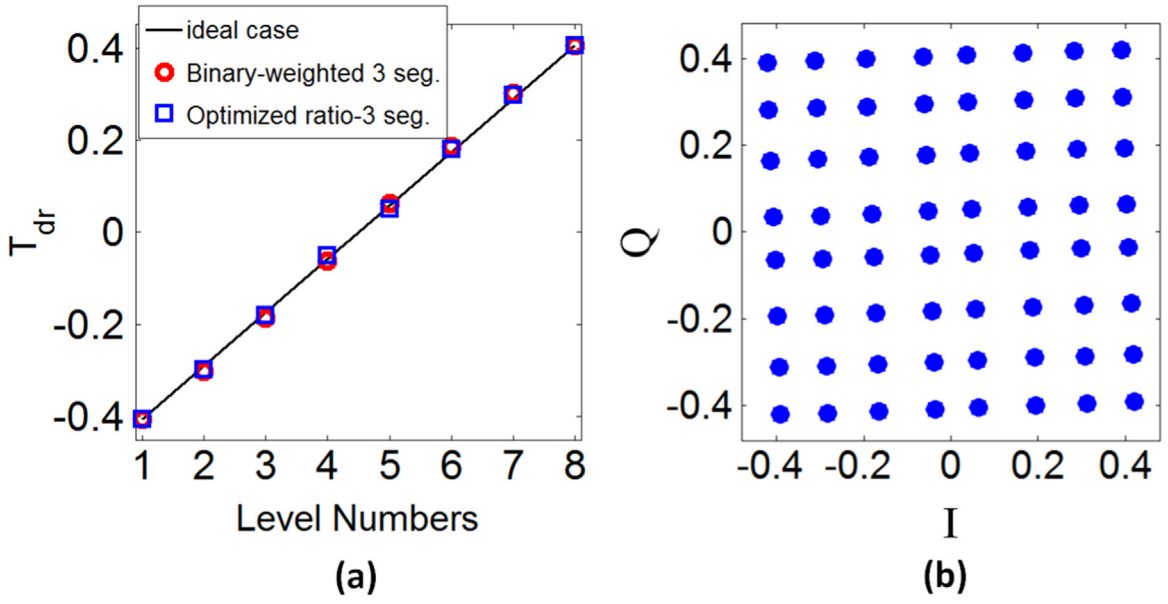

Fig. 10. (a) Field transmission at the drop port of the MZIARM plotted for each level assuming binary-weighted and optimized ratio 3-segment case in depletion mode. The ideal case is also plotted with a solid line. (b) QAM-64 constellation for the 3-segment IQ modulator with optimized segment lengths.

(Fig. 5b), the level distribution might be close to the ideal case. In Fig. 10a, an ideal line connecting T_{dr} at Level 1 to T_{dr} at Level 8 for the 3-segment add-drop MZIARM is plotted. Also shown with circles are the T_{dr} values for each level when $r_2 = 2$ and $r_3 = 4$ in the binary-weighted case. These values are close to the ideal case.

In order to quantize the level nonlinearity, we use differential nonlinearity (DNL) and integral nonlinearity (INL) as in [19]. In this case, DNL shows deviation of the actual level difference ($T_{dr_{m+1}} - T_{dr_m}$, m be a level number) from ideal linear level difference (T_{LSB}) in unit of the least significant bit (LSB) and is defined as follows:

$$DNL = \left| \frac{T_{dr_{m+1}} - T_{dr_m}}{T_{LSB}} - 1 \right|. \tag{8}$$

INL quantizes the maximum amount of deviation of the actual output levels, T_{dr_m}, from a fitted line in unit of LSB and is calculated from

$$INL = \frac{T_{dr_m} - T_{dr_1} - S \times (m-1)}{T_{LSB}}, \tag{9}$$

where S is the slope of the fitted line. For the binary-weighted case shown in Fig. 10a, the value of INL and DNL is calculated to be 0.11 and 0.1 LSB, respectively.

In order to improve linearity, the optimized r_2 and r_3 are calculated such that the root-mean-square error (RMSE) with respect to the ideal line (Fig. 10a), is minimized. The T_{dr} values for this optimized case which occur when r_2 and r_3 are around 1.96 and 3.72, respectively, are plotted in Fig. 10a as squares. For this case INL and DNL are calculated to be 0.07 and 0.13 LSB, respectively. Therefore, linearity is improved to a small degree compared to the binary weighting case. The QAM-64 constellation for this case is illustrated in Fig. 10b.

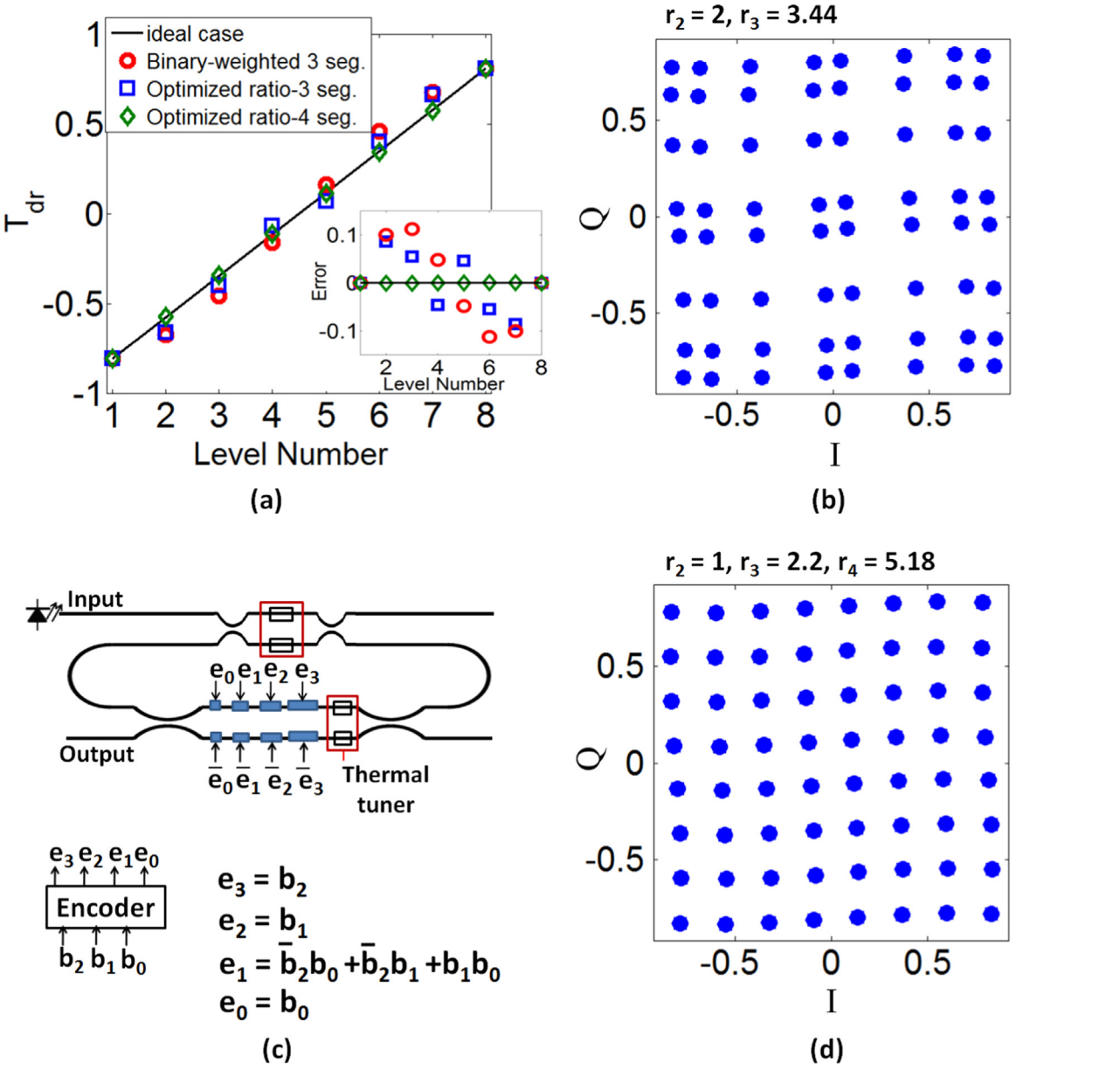

Fig. 11. (a) Field transmission at drop port of the MZIARM plotted for each level for binary-/optimized-weighted 3-segment and for optimized-weighted 4-segment case assuming pin forward-biased RF section with $L_t = 100\,\mu m$. (b) QAM-64 constellation for the 3-segment IQ modulator with optimized segment lengths. (c) 4-segment MZIARM proposed for the properly aligned QAM-64 constellation. Encoder table for mapping a 3-bit input to a 4-bit input is also shown. (d) QAM-64 constellation for the 4-segment IQ modulator with optimized segment lengths.

To increase distance between points in QAM constellation, it might be necessary to move further up in $|T_{dr}|$–$\Delta\phi/\pi$ curve where the nonlinearity is more significant for this larger dynamic range. To achieve this, in the current example, either L_t or the applied voltage should be increased. Alternatively, an active region with smaller $V_\pi \cdot L$, such as forward-biased junctions, could be chosen. To demonstrate how to achieve linearly-distributed levels when dynamic range covers nonlinear section of the transmission curve, a QAM-64 signaling is examined using forward-biased pin junction with $L_t = 100$ μm for 1 V_{PP}. As the carrier injection is more efficient to induce effective index change compared with carrier depletion [20], the device could be smaller in size, but with the disadvantage of being bandwidth limited. The T_{dr} distribution for the binary-weighted and the optimized-weighted 3-segments with $r_2 = 2$ and $r_3 = 3.44$ are plotted in Fig. 11a where the optimized case shows a clear improvement. The inset of Fig. 11a shows the error which is defined as the distance between the ideal T_{dr} to the T_{dr} achieved for each level number. The improvement of the optimized segment length to the binary-weighted segment length is more clear. Also, INL decreases from 0.49 LSB in the binary case to 0.37 LSB in the optimized case while DNL stays almost the same at around 0.4 LSB. The QAM-64 constellation corresponding to this optimized case is also plotted in Fig. 11b, which shows more improvement is required.

To improve the linearity further and compensate the transmission nonlinearity in this dynamic range, similar to the segmented MZI [21], an extra segment can be added while keeping L_t constant. Using this extra segment, another parameter is added as $r_4 = L_4/L_1$ and the aforementioned 4 equations from Eq. (7) can be solved for exact linearity. In this case, an encoder is required to map the 3-bit input of b_2, b_1 and b_0 to 4 bits of e_3, e_2, e_1 and e_0 as shown in Fig. 11c. The T_{dr} distribution for the calculated $r_2 = 1$, $r_3 = 2.2$, and $r_4 = 5.18$ based on the encoder equations shown in Fig. 11c, is plotted in Fig. 11a as diamonds which fall exactly on the ideal line. This is more clear from the inset of Fig. 11a. The QAM-64 constellation for this 4-segment add-drop MZIARM IQ modulator is plotted in Fig. 11d which demonstrates perfect linearity.

From both constellations in Figs. 10b and 11d, it is clear that constellation points deviation from vertical and horizontal lines is due to the aforementioned phase error. The maximum phase error in the forward bias case is about 0.12π, which is $6\times$ larger than the corresponding error in the reverse-bias case (due to a more severe loss modulation with voltage). However, in the forward bias case, the larger distance between the points in constellation may compensate for this larger phase error, resulting in the same bit error rate.

According to Fig. 4 and aforementioned discussions, the advantages of smaller footprint and lower required driving voltage of the proposed QAM architecture compared with the architecture using MZI are more significant when the loss and/or device length become smaller. Hence, to obtain maximum efficiency of the proposed device, it is necessary to select a technology with high efficiency in electro-optical modulation and with low loss in passive and active regions. Here, we chose lateral pn/pin junction to show the proof of concept. Using SISCAP [21] or interleaved pn junction [22] for implementing this device will lead to a smaller device with lower drive voltage requirement due to their smaller $V_\pi \cdot L$ compared with that of a lateral pn junction. Although, the bandwidth of the device with interleaved pn junction may degrade compared with the one with a lateral pn junction, it is still well above the forward-biased pin device [23].

6. Conclusion

We proposed and analyzed a DAC-free pure optical QAM-2^{2N} modulator using two N-segment MZIARMs in the conventional IQ scheme. The proposed modulator has the advantages of being driven with binary signal, having small number of modulators, smaller size, and lower required applied voltage compared to the devices previously proposed. The loss in MZI was taken into account and we showed that loss imbalance in MZI arms generates phase error in advance modulation formats such as QAM. The proposed QAM modulator transient response was also assessed in non-quasi-static mode of operation. The effect of the nonlinear transfer function curve of the device was studied both for QAM-16 and QAM-64. The impact of various design parameters on the constellation map was investigated. To achieve the properly aligned constellation, number of segments and their length should be optimized.

Acknowledgment

Authors are grateful for the financial support of the Natural Sciences and Engineering Research Council of Canada. Authors would also like to thank Dr. Nima Zareian for thoughtful and constructive comments.

References

[1] G. Li, Recent advances in coherent optical communication, Adv. Opt. Photon. 1 (2) (2009) 279–307.
[2] K.P. Ho, H.W. Cuei, Generation of arbitrary quadrature signals using one dual-drive modulator, J. Lightwave Technol. 23 (2) (2005) 764.
[3] M. Seimetz, High-Order Modulation for Optical Fiber Transmission, vol. 143, Springer-Verlag, Berlin, Heidelberg, 2009 http://dx.doi.org/10.1007/978-3-540-93771-510.1007/978-3-540-93771-5⟩.
[14] W.D. Sacher, J.K.S. Poon, Characteristics of microring resonators with waveguide-resonator coupling modulation, J. Lightwave Technol. 27 (2009) 3800.
[15] A. Yariv, P. Yeh, Photonics: Optical Electronics in Modern Communications, Oxford University Press Inc., New York, NY, USA, 2006.
[16] ⟨https://www.lumerical.com⟩.
[17] X. Zheng, Y. Luo, G. Li, I. Shubin, H. Thacker, J. Yao, K. Raj, J.E. Cunningham, A. V. Krishnamoorthy, Enhanced optical bistability from self-heating due to free carrier absorption in substrate removed silicon ring modulators, Opt. Express 20 (10) (2012) 11478–11486.
[18] T. Kawanishi, T. Sakamoto, V. Chiba, M. Izutsu, Study of precise optical modulation using Mach–Zehnder interferometers for advanced modulation formats, IEEE ECOC (2007) 1–2.
[19] Y. Ehrlichman, O. Amrani, S. Ruschin, Improved digital-to-analog conversion using multi-electrode Mach–Zehnder interferometer, J. Lightwave Technol. 26 (21) (2008) 3567–3575.
[20] Q. Xu, S. Manipatruni, B. Schmidt, J. Shakya, M. Lipson, 12.5 Gbit/s carrier-injection-based silicon micro-ring silicon modulators, Opt. Express 15 (2) (2007) 430–436.
[21] X. Wu, B. Dama, P. Gothoskar, P. Metz, K. Shastri, S. Sunder, J. Van der Spiegel, Y. Wang, M. Webster, W. Wilson, A 20 Gb/S NRZ/PAM-4 1V transmitter in 40 nm CMOS driving a Si-photonic modulator in 0.13 μm CMOS, IEEE ISSCC (2013) 128–129.
[22] Z. Li, D. Xu, W. McKinnon, S. Janz, J. Schmid, P. Cheben, J. Yu, Silicon waveguide modulator based on carrier depletion in periodically interleaved PN junctions, Opt. Express 17 (18) (2009) 15947–15958.
[23] H. Yu, M. Pantouvaki, J. Van Campenhout, D. Korn, K. Komorowska, P. Dumon, Y. Li, P. Verheyen, P. Absil, L. Alloatti, D. Hillerkuss, J. Leuthold, R. Baets, W. Bogaerts, Performance tradeoff between lateral and interdigitated doping patterns for high speed carrier-depletion based silicon modulators, Opt. Express 20 (12) (2012) 12926–12938.